Research Article | Vol. 32, No. 13 / 17 Jun 2024 / Optics Express 23204

Optics EXPRESS

Adaptive multi-band modulation for robust and low-complexity faster-than-Nyquist non-orthogonal FDM IM-DD systems

PEIJI SONG,[1] ZHOUYI HU,[2,*] YUAN LIU,[1] YIZHAN DAI,[1] CHAO GAO,[3] AND CHUN-KIT CHAN[1]

[1] *Department of Information Engineering, The Chinese University of Hong Kong, Shatin, N. T., Hong Kong SAR, China*
[2] *Key Laboratory of All-Optical Networks and Modern Communication Networks of Ministry of Education, Institute of Lightwave Technology, Beijing Jiaotong University, Beijing 100044, China*
[3] *Department of Electronic Engineering, The Chinese University of Hong Kong, Shatin, N. T., Hong Kong SAR, China*
[*] *zyhu@bjtu.edu.cn*

Abstract: Faster-than-Nyquist non-orthogonal frequency-division multiplexing (FTN-NOFDM) has been shown to have good robustness against the steep frequency roll-off in a bandwidth-limited optical communication system. Among various FTN-NOFDM techniques, the non-orthogonal matrix precoding (NOM-p) based FTN has relatively high compatibility, which can easily utilize the existing advanced digital signal processing (DSP) techniques in the conventional OFDM. In this work, we propose what we believe to be a novel FTN-NOFDM scheme with adaptive multi-band modulation. By dividing the single-band NOM-p into multiple-band NOM-p, the proposed scheme is able to assign different quadrature amplitude modulation (QAM) levels to different sub-bands, leading to better utilization of the low-pass-like channel as well as reduced computational complexity. The impacts of sub-band number and bandwidth compression factor on the bit-error-rate (BER) performance and complexity are experimentally analyzed in a 32.23-Gb/s and 20-km intensity modulation-direct detection (IM-DD) optical transmission system. Results show that the proposed scheme with a proper sub-band number can lower the BER and greatly reduce the complexity compared to the conventional single-band scheme.

1. Introduction

Intensity modulation-direct detection (IM-DD) optical transmission is a promising solution for short-reach applications such as data center networks [1,2], visible light communications (VLCs) [3], and passive optical networks [4] due to its low cost and simple implementation complexity. However, the steep frequency roll-off along the spectral response caused by either (i) the interaction between chromatic dispersion (CD) and square-law detection or (ii) the bandwidth limitation of transceiver components significantly limits the IM-DD system's transmission performance. The orthogonal frequency division multiplexing (OFDM) technique is a popular technique to combat it in the following two ways: (i) fully making use of the channel characteristics with bit-loading (BL) [5,6] and (ii) attaining a flat signal-to-noise-ratio (SNR) profile over all subcarriers based on orthogonal matrix precoding/decoding [7,8]. The former is capacity-approaching but requires additional round-trip delay to evaluate the accurate channel state information (CSI), while the latter can improve the performance without requiring CSI, which has been extensively studied [7,8].

Recently, by further reducing frequency spacing between neighboring subcarriers beyond the Nyquist limit, the faster-than-Nyquist non-orthogonal frequency-division multiplexing (FTN-NOFDM), also termed spectrally efficient frequency division multiplexing (SEFDM) in literature,

#526164 https://doi.org/10.1364/OE.526164
Journal © 2024 Received 15 Apr 2024; revised 16 May 2024; accepted 22 May 2024; published 10 Jun 2024

was proposed to be more robust against the steep frequency roll-off because of the ability of spectrum compression [9–18]. Though it is possible to combine BL with FTN-NOFDM [15,16], this scheme is channel-dependent, which needs precise CSI and requires complex coding and decoding procedures, restricting the implementation of FTN-NOFDM for time-varying channels. On the other hand, built on the aforementioned orthogonal matrix precoding/decoding, the non-orthogonal matrix precoding (NOM-p)-based FTN-NOFDM system proposed in Ref. [10] and [12] independently is regarded to be advantageous due to its high flexibility and compatibility with the conventional OFDM. Therefore, the existing digital signal processing (DSP) techniques, such as zero-forcing (ZF)-based channel estimation/equalization, can be easily utilized in such an FTN-NOFDM system without any modification. Moreover, the NOM-p-based FTN-NOFDM can also flatten the SNR profile like the orthogonal matrix precoding/decoding-based OFDM [10], which further enhances the system robustness against the steep frequency roll-off. However, only the single-band case has been investigated in previous works, which was inefficient for performance optimization with the NOM-p FTN-NOFDM technique.

In this work, we propose an adaptive multi-band modulation FTN-NOFDM technique by dividing the single-band NOM-p into multiple-band NOM-p, where different quadrature amplitude modulation (QAM) levels are applied to different sub-bands, effectively utilizing the low-pass-like channel and reducing the complexity. Different from the conventional multi-band scheme using orthogonal matrix precoding/decoding [19], the proposed multi-band NOM-p in this work can further improve the system's tolerance to frequency roll-off with additional bandwidth saving. We experimentally study the impacts of sub-band number and bandwidth compression factor on the bit-error-rate (BER) performance and complexity in a 32.23-Gb/s and 20-km IM-DD optical transmission system. Experimental results show that the proposed scheme with an appropriate sub-band number can significantly lower the BER and reduce the FTN decoding complexity compared to the conventional single-band scheme.

Notations: Unless otherwise specified, vectors are denoted by boldfaced small letters, e.g., $\boldsymbol{x}$, while matrices are expressed by capital letters, e.g., $\boldsymbol{X}$. x_i denotes the i-th element of $\boldsymbol{x}$, $\boldsymbol{X}_{i,n}$ is the element located on the i-th row and the n-th column of $\boldsymbol{X}$, and s_i^L is the i-th element of the L-th segment of vector $\boldsymbol{s}$.

2. Principles

2.1. Adaptive multi-band modulation FTN-NOFDM technique

Figure 1 depicts the comparison between the sketched spectra of OFDM and FTN-NOFDM. The subcarrier spacing of FTN-NOFDM is equal to the original spacing in the conventional OFDM being compressed by the bandwidth compression factor α (<1). Hence, the system's robustness against the steep frequency roll-off can be enhanced with such bandwidth saving.

The inverse fractional Fourier transform (IFrFT) is usually used to generate the FTN-NOFDM signal. The time-domain samples of one FTN-NOFDM symbol can be written as [17]

$$x[k] = \sum\nolimits_{v=1}^{V} s_v \exp\left(\frac{j2\pi(v-1)(k-1)\alpha}{V}\right),\ k = 1, 2, \cdots, V, \tag{1}$$

where $\boldsymbol{s} = [s_1, s_2, \cdots, s_V]$ denotes the mapped QAM symbols in the frequency domain, V is the number of subcarriers, and α (<1) is the compression factor. With IFrFT, the orthogonality among subcarriers is purposely violated to achieve an FTN rate. Unfortunately, the IFrFT also changes the frequency distribution of subcarriers, preventing the real-valued signal from being generated by simple Hermitian symmetry. As reported in [18], the digital up-conversion is applied to the complex-valued FTN-NOFDM signal for executing intensity modulation. However, the additional guard band is induced between the optical carrier and the carried signal, which sacrifices part of the robustness contra narrow-bandwidth filtering. Besides, channel estimation/equalization remains a crucial problem due to the loss of the orthogonality among subcarriers. Though the

Optics EXPRESS

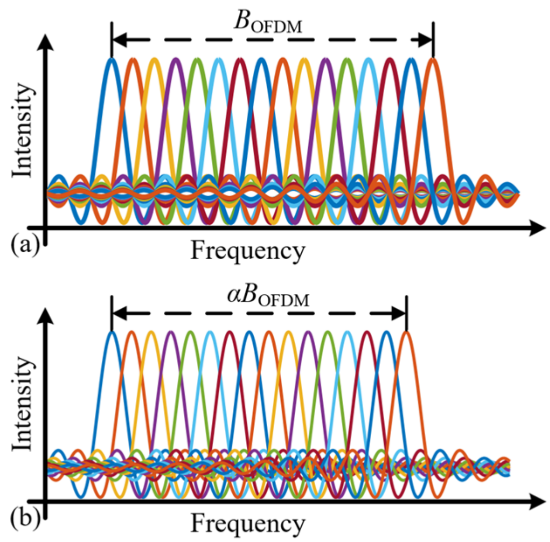

Fig. 1. The sketched spectra of (a) OFDM and (b) FTN-NOFDM (α=0.9).

frequency-domain channel estimation/equalization method proposed in [20] can help alleviate this problem, one pair of additional IDFT/DFT is required, and there will be a frequency offset, resulting in higher implementation complexity and potentially degraded performance when there exists power leakage.

To make the channel estimation/equalization of FTN-NOFDM compatible with the conventional OFDM modulator without performance degradation, NOM-p FTN-NOFDM scheme was proposed [10,12], which shifts the compression process and performs it before the OFDM modulation. Figure 2 shows the generation of FTN-NOFDM signal utilizing the NOM-p, where $L = 1$ corresponds to the conventional single-band scheme, and $L \geq 2$ corresponds to the proposed adaptive multi-band modulation by evenly partitioning the single band into multiple sub-bands.

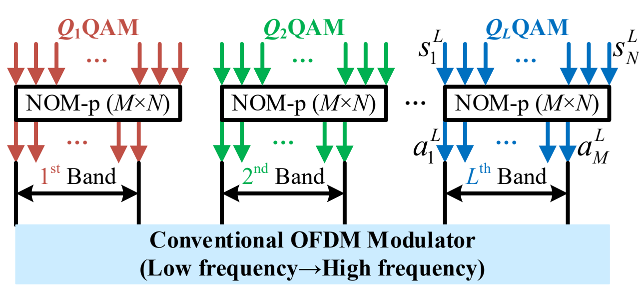

Fig. 2. Principle of the proposed adaptive multi-band NOM-p FTN-NOFDM scheme, where $L = 1$ corresponds to the conventional single-band case.

Since the single band is a special case of multiple sub-bands when $L = 1$, the L-th sub-band in Fig. 2 is used as an example to illustrate the concept of NOM-p FTN-NOFDM. The N subcarriers (e.g., (s_1^L, ⋯, s_N^L) for the L-th sub-band) are squeezed into M subcarriers (e.g., (a_1^L, ⋯, a_M^L) for the L-th sub-band) via an $M \times N$ non-orthogonal matrix (NOM) $\boldsymbol{F}$, where $N = V/L$. The bandwidth compression factor α in this process is defined by α=M/N, corresponding to $(1-\alpha) \times 100\%$ of the bandwidth saved. The NOM $\boldsymbol{F}$ is generated by an $N \times N$ orthogonal matrix

Optics EXPRESS

with $N-M$ rows discarded, which could be a standard discrete Fourier transform (DFT) matrix, an orthogonal circulant transform (OCT) matrix, or other suitable orthogonal precoding matrices [7,8]. Without loss of generality, we use an $N \times N$ OCT matrix [21] in this work, which is given by $\boldsymbol{W} = (1/\mathrm{sqrt}(N)) \times [c_1, c_2, \cdots, c_N; c_N, c_1, \cdots, c_{N-1}; \cdots; c_2, c_3, \cdots, c_1]$, where c_i $(1 \le i \le N)$ in $\boldsymbol{W}$ is the corresponding element of a Zadoff-Chu (ZC) sequence [22] with the sequence index of 1 and a length of N. Therefore, $\boldsymbol{F}$ can be obtained from $\boldsymbol{W}$ by discarding $N-M$ rows. After applying NOM-p to all L sub-bands, the obtained $L \times M$ subcarriers are allocated onto the orthogonal subcarriers from low to high-frequency zones in a standard IDFT-based OFDM modulator. As a result, the NOM-p FTN-NOFDM signal shows a similar behavior as the conventional OFDM signal, making it compatible with OFDM-related DSP, e.g., the simple ZF channel estimation/equalization.

Figure 3(a) shows the profile of a simulated channel realized by a 4-th-order Butterworth filter. Figure 3(b) gives the comparison of SNR curves of different schemes through simulation, where L was set to 3 for the multi-band schemes as an example. It can be seen that the conventional OFDM signal suffers from serious frequency roll-off, while the multi-band OFDM/FTN-NOFDM can achieve ladder-like SNR curves, thus improving system resistance to steep frequency roll-off by applying different QAM levels to different sub-bands. Furthermore, the multi-band FTN-NOFDM lifts the SNR of each sub-band compared to the conventional multi-band OFDM due to the discarded poor subcarriers that are located at the high-frequency region, indicating its advantage. Meanwhile, there is only little penalty from Multi-band-FTN when α is not too small, as shown in this example (α=0.9).

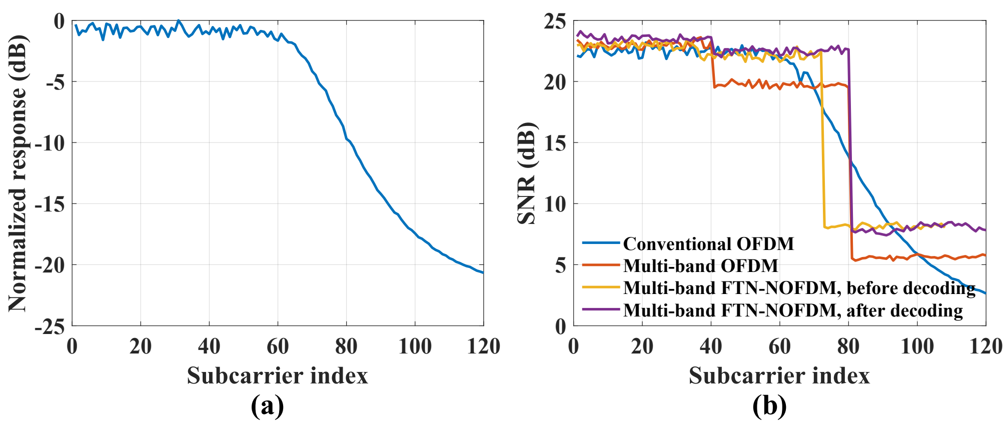

Fig. 3. (a) The channel response of the used 4-th-order Butterworth filter; (b) The comparison of SNR curves for different schemes, where the SNR was set to 21 dB, the compression factor α=0.9 for the multi-band FTN-NOFDM, and the total number of subcarriers $V = 120$.

In this work, the original subcarriers are modulated with uniform 8QAM for the single-band case, where the circular constellation is used, due to its superior performance in both OFDM and FTN-NOFDM systems [23]. For the multi-band case, considering a low-pass property of an IM-DD optical channel, which is feasible in most cases of practical applications, spectral efficiency is assigned to the sub-bands in descending order, i.e., the QAM order Q_l for $l = 1, \cdots, L$ satisfies $Q_1 \ge Q_2 \ge \cdots \ge Q_L$ to make more rational use of the channel. Therefore, to ensure the same data rate, we set $[Q_1, Q_2] = [16,4]$ for the 2-band case, $[Q_1, Q_2, Q_3] = [16,8,4]$ for the 3-band case, $[Q_1, Q_2, Q_3, Q_4] = [16,16,4,4]$ or $[16,16,8,2]$ for the 4-band case, and $[Q_1, Q_2, Q_3, Q_4, Q_5] = [16,16,8,4,4]$ for the 5-band case, respectively.

Optics EXPRESS

2.2. Detection of FTN-NOFDM signal

At the receiver side, the received signal of the L-th sub-band after equalization and inverse NOM-p can be written as

$$y_n^L = \boldsymbol{C}_{n,n} s_n^L + \sum\nolimits_{i=1, i \neq n}^{N} \boldsymbol{C}_{n,i} s_i^L + z_n^L,\ n = 1,\ \ldots,\ N, \tag{2}$$

where $\boldsymbol{C}$ is the $N \times N$ ICI matrix, whose element in the position of the n-th row and the i-th column can written as

$$\boldsymbol{C}_{n,i} = \boldsymbol{F}(n,\ :)\boldsymbol{F}^{\mathrm{H}}(:,\ i),\ n,\ i = 1,\ \ldots,\ N. \tag{3}$$

where $\boldsymbol{F}(n, :)$ and $\boldsymbol{F}(:, i)$ are the n-th row and the i-th column of $\boldsymbol{F}$, respectively, and $(\cdot)^{\mathrm{H}}$ denotes the Hermitian transpose.

z_n^L is the zero-mean additive white Gaussian noise with a variance of σ_L^2 for the L-th sub-band. Due to the noise-spreading effect of NOM-p as shown in Fig. 3(b), the noise variance per subcarrier within the same sub-band is set to be the same, which is calculated as

$$\sigma_L^2 = \frac{1}{N} \sum\nolimits_{m=0}^{M-1} \sigma_{L,m}^2, \tag{4}$$

where $\sigma_{L,m}^2$ is the estimated noise variance on the m-th subcarrier of the L-th sub-band prior to the inverse NOM-p.

The inter-carrier interference (ICI) is produced from the NOM-p when $M<N$. Taking both noise and ICI into consideration, the logarithmic-maximum-a-posterior (log-MAP) Viterbi decoding algorithm shows superior performance in reducing the ICI because of its maximum likelihood (ML) performance [11]. The key idea of the log-MAP Viterbi decoding algorithm is that it jointly detects the first P symbols sequentially, where P increases from 1 to N and a certain number of search paths are saved for each value of P. The logarithmic-a-posteriori-probability (log-APP) of the joint detection on the first P ($P = 1, 2, \cdots, N$) symbols s_n^L, $n = 1, 2, \cdots, P$, which serves as the metric determining the retained paths, is given by

$$Pr = -\boldsymbol{d}^{\mathrm{H}} \boldsymbol{\Gamma}^{-1} \boldsymbol{d}, \tag{5}$$

$$d_n^L = y_n^L - \sum_{i=1}^{P} \boldsymbol{C}_{n,i} s_i^L, \tag{6}$$

$$\boldsymbol{\Gamma}_{n,i} = \begin{cases} \sum\limits_{n=1}^{P} \sum\limits_{i=1}^{P} \sum\limits_{g=P+1}^{N} \boldsymbol{C}(n,g)\boldsymbol{C}^{\mathrm{H}}(i,g) + \boldsymbol{A}_{n,i}, & P<N \\ \boldsymbol{A}_{n,i}, & P = N \end{cases}, \tag{7}$$

where $\boldsymbol{A}$ is the $P \times P$ diagonal matrix whose diagonal elements are σ_L^2. For the details, please refer to [11].

The Viterbi decoding scheme is exploited to reduce the complexity during the sequential decoding that P increases from 1 to N, where the number of the pre-set surviving paths in Viterbi decoding is represented as B. Taking the binary phase-shift keying (BPSK) format and $B = 2$ as an example, Fig. 4 gives decoding procedures using the tree diagram. For each P jointly detected symbol (the P-th row in the tree diagram), two ML paths are retained (indicated as solid dots of the tree diagram) from all candidates (all dots in the P-th row of the tree diagram).

Optics EXPRESS

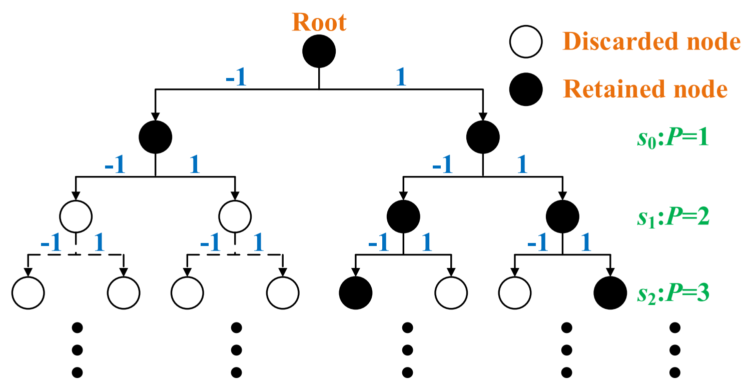

Fig. 4. Tree diagram of the log-MAP Viterbi decoding algorithm, where the number of surviving path in each layer is 2. The solid dots denote the retained ML detections, while the others denote the discarded ones.

2.3. Complexity analysis

The computational complexity of one sub-band containing NOM-p, inverse NOM-p, and log-MAP Viterbi decoding algorithm is analyzed below in terms of complex multiplication (CM) and complex addition (CA): (i) for NOM-p, each sub-band requires MN CM and $M(N-1)$ CA; (ii) for inverse NOM-p, each sub-band requires NM CM and $N(M-1)$ CA; (iii) for the log-MAP Viterbi decoding algorithm, its complexity is mainly induced by Eqs. (5)-(7), thus the produced CM and CA when calculating one path for a given P in the Viterbi decoding are:

$$\mathrm{CM} = \begin{cases} -P^3 + (N+2)P^2 + P, & P<N \\ 2N^2 + N, & P = N \end{cases}, \tag{8}$$

$$\mathrm{CA} = \begin{cases} -P^3 + (N+2)P^2 - 1, & P<N \\ 2N^2 - 1, & P = N \end{cases}. \tag{9}$$

Considering that the number of paths to be calculated is Q when $P = 1$, and BQ when $P \geq 2$, the total complexity induced by the log-MAP Viterbi decoding algorithm to get the final ML detection of the N symbols for one sub-band is

$$CM = \frac{1}{12}(BQN^4 + 8BQN^3 + 17BQN^2 + (12Q - 2BQ)N + 24Q - 24BQ), \tag{10}$$

$$CA = \frac{1}{12}(BQN^4 + 8BQN^3 + 11BQN^2 + (12Q - 20BQ)N). \tag{11}$$

Since the log-MAP Viterbi decoding algorithm with $B = Q$ can yield a saturate performance close to the ML one [11], we set $B = Q$ in this work. Then, the total complexity induced from NOM-p, inverse NOM-p, and log-MAP Viterbi decoding algorithm for one sub-band can be calculated by

$$CM = \frac{1}{12}(Q^2N^4 + 8Q^2N^3 + 17Q^2N^2 + (12Q - 2Q^2)N + 24Q - 24Q^2 + 24MN), \tag{12}$$

$$CA = \frac{1}{12}(Q^2N^4 + 8Q^2N^3 + 11Q^2N^2 + (12Q - 20Q^2)N + 24MN - 12M - 12N). \tag{13}$$

In order to intuitively embody the merit of the proposed scheme in reducing complexity, Fig. 5 depicts the results of CM and CA versus the number of sub-band L for one FTN-NOFDM symbol

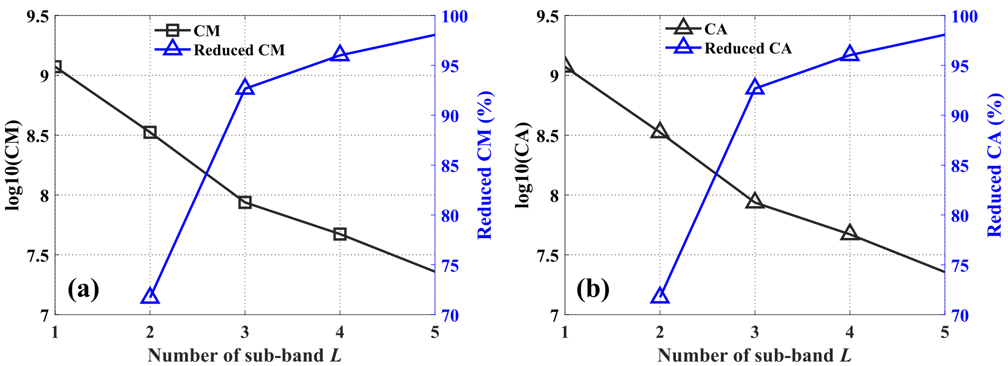

Fig. 5. The computational complexity versus the number of sub-band L for one FTN-NOFDM symbol for (a) the CM, and (b) the CA.

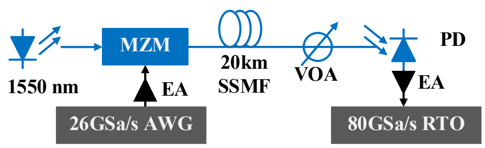

TxDSP	RxDSP
Bit stream	Resample (80GSa/s)
QAM mapping	Serial-to-parallel
Adaptive modulation	CP removal
Hermitian symmetry	256-point FFT
256-point IFFT	1-tap equalization
8-point cyclic prefix	Symbol decision
Parallel-to-serial	BER

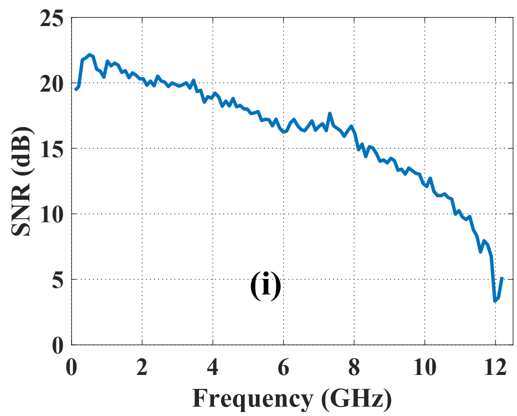

Fig. 6. Experimental setup and DSP flow chart (AWG: arbitrary waveform generator, EA: electrical amplifier, MZM: Mach-Zehnder modulator, SSMF: standard single-mode fiber, VOA: variable optical attenuator, PD: photodiode, RTO: real-time oscilloscope). Inset (i): measured SNR profile after 20-km SSMF transmission.

when the total number of subcarriers $V = 120$, where the QAM levels assigned to each sub-band follow the description in Section 2.1 and $[Q_1, Q_2, Q_3, Q_4] = [16,16,4,4]$ for $L = 4$ due to its better performance to be illustrated later. It can be found that the exponential part of the complexity decreases as L increases, and the required CM and CA are almost equal. Specifically, when $L = 2$ and $L > 3$, the needed CM and CA are both reduced by more than 70% and 90%, respectively.

3. Experimental setup

Figure 6 shows the experimental setup and the corresponding DSP. The offline-generated digital signal using MATLAB was first transformed into an analog signal by an arbitrary waveform generator (AWG), whose peak-to-peak voltage (Vpp) was optimized at 300 mV during this experiment. Subsequently, the output signal was amplified by an electrical amplifier (EA). A Mach-Zehnder modulator (MZM) combined with an external cavity laser (ECL) at 1550 nm converted the electrical signal to the optical domain. After 20-km standard single-mode fiber (SSMF) transmission, the signal was detected by a receiver module consisting of a photodiode (PD) and an EA. Finally, a real-time oscilloscope (RTO) captured the detected signal which was processed by offline DSP. Inset (i) on the right side of Fig. 6 gives the SNR profile

Optics EXPRESS

after transmission, showing that the SNR reduces quickly when the frequency exceeds 10 GHz. Figure 7 shows the electrical spectra of the received FTN-NOFDM signal with different bandwidth compression factors. It can be seen from Fig. 7 that the signal cutoff bandwidth was compressed from 12.18 GHz to 10.97 GHz, and 9.75 GHz when α was set to 0.9, and 0.8, respectively.

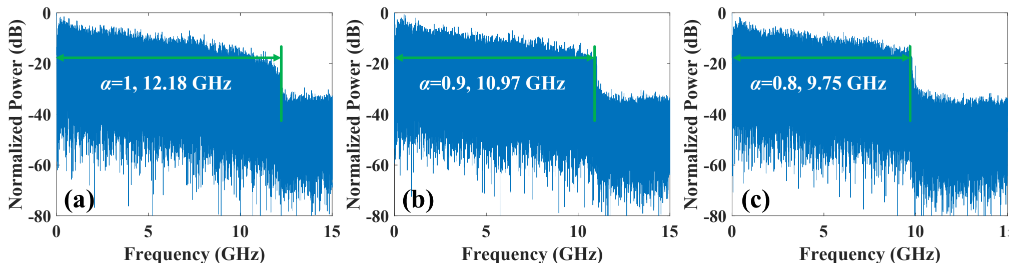

Fig. 7. The electrical spectra of the received FTN-NOFDM signals with a compression factor α of (a) 1, (b) 0.9, and (c) 0.8, respectively.

For a fair comparison, the original total number of subcarriers (V) was fixed at 120, carrying 360 bits (equivalent to 3 bits/subcarrier) in total. The IFFT size was set to 256, and the cyclic prefix (CP) length was 8. 20 blocks of 4QAM OFDM training symbols (TS) were added before 200 blocks of payload FTN-NOFDM symbols for equalization. The AWG (Keysight M8199A) worked at 26GSa/s, and the RTO (Keysight DSAV334A) worked at 80GSa/s in this work. Therefore, the data rate of the signal excluding CP and TS was 32.23 ($\approx 26 \times 3 \times 120/(256+8) \times 200/220$) Gb/s.

4. Experimental results

Figure 8 shows the experimental results. We first study the BER performance of the proposed adaptive multi-band modulation with different L and α values, as shown in Fig. 8(a), where the numbers inside square brackets in the legend represent the QAM levels allocated to each sub-band. It can be noticed from Fig. 8(a) that there is a different optimum α value for different cases. Because the system is bandwidth-limited, appropriate bandwidth saving can help alleviate the negative effect of the steep frequency roll-off. However, when α further decreases, the penalty of the increased ICI becomes dominant, reducing the overall BER performance. Based on the results in Fig. 8(a), we compare the lowest achievable BER of different sub-band numbers L in Fig. 8(b). We can see that except for $L=4$, multi-band signals can outperform the conventional single-band NOM-p-based FTN signal ($L=1$); among them, $L=3$ performs the best in this work. It is worth noting that since the BER of each sub-band is determined by its SNR as well as the assigned modulation format, and the average BER is dominated by the worst BER among all sub-bands, the average BER fluctuates with different number of sub-bands, which is an inherent property of this approach. In addition, although $L=3$ is the optimal sub-band number in this work, it could be optimized to other values according to the specific transmission channel and data rate requirements. Based on the complexity analysis in Section 2.3, the complexity reductions from applying the proposed multi-band scheme with $L=3$ in complex multiplication and complex addition are 92.65% and 92.67%, respectively.

To further investigate why $L=3$ leads to better performance, Table 1 presents the BER of each subband when $L=1$, 2, 3, 4, and 5, where $[Q_1, Q_2, Q_3, Q_4] = [16,16,4,4]$ for $L=4$ due to its better performance than $[Q_1, Q_2, Q_3, Q_4] = [16,16,8,2]$. We can see from the table that $L=3$ can achieve more uniform BERs than other cases. Since the average BER is dominated by the worst BER among them, this inspires us that optimizing for a suitable sub-band number as well as QAM format allocation can achieve a relatively flat BER distribution, which is vital for better transmission performance.

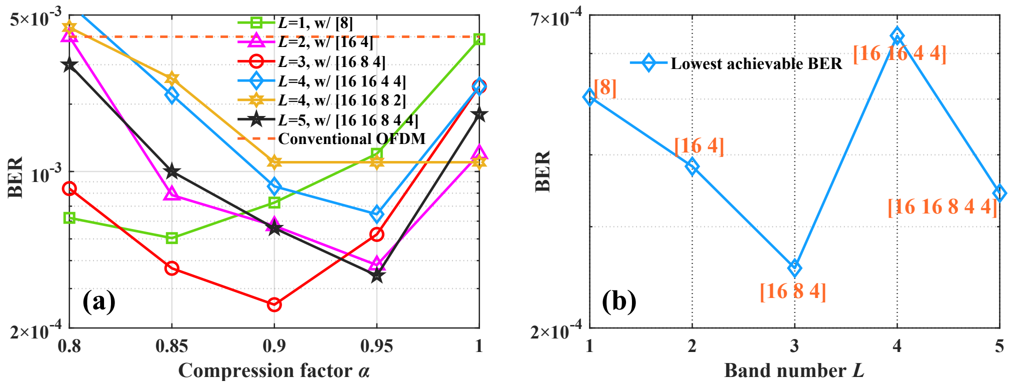

Fig. 8. (a) The BER versus the number of sub-bands (L) with different compression factors (α), and (b) the lowest achievable BER under different L values.

Table 1. Expanded BER per sub-band from Fig. 8(b)

Band Number \ Band Index	1	2	3	4	5
1	5.04×10^{-4}				
2	4.6×10^{-4}	2.25×10^{-4}			
3	2.6×10^{-4}	1.75×10^{-4}	3.62×10^{-4}		
4	1×10^{-4}	1.4×10^{-3}	0	8×10^{-4}	
5	1×10^{-4}	6×10^{-4}	2×10^{-4}	0	1×10^{-3}

The results shown in Fig. 8 have verified that the system performance can be further improved by the proposed adaptive multi-band modulation scheme, due to the achieved ladder-like SNR profile and the saved signal bandwidth. The optimization of the compression factor α is the generality of an FTN system, and it is different from the bit and power loading algorithm which requires precise CSI [5].

Finally, we have measured the received optical power (ROP) sensitivity curves as presented in Fig. 9(a), where L is set to 3 in the proposed scheme for its best performance in this work. Besides, we also measured the BER performance of BL with Chow's algorithm to provide a benchmark, whose bit allocation result at ROP $= -1$ dBm is shown in Fig. 9(b). It can be found that compared with the conventional OFDM, the proposed method can improve the ROP sensitivity by ~1.8 dB at the HD-FEC threshold (3.8×10^{-3}). Meanwhile, although it shows slightly worse performance than the BL scheme at the HD-FEC threshold, the proposed method outperforms the BL scheme at the KP4-FEC threshold (2.2×10^{-4}) by ~0.8 dB at the high ROP region, which can be attributed to the saving of 10% bandwidth located at the high frequency (worst SNR). It also should be noted that the proposed scheme does not require precise CSI for frequent optimization, simplifying the system complexity compared with BL. Nevertheless, since the performance of log-MAP Viterbi decoding algorithm decreases as the noise increases [10,11], FTN-NOFDM performs worse than both BL and the conventional OFDM at the low ROP region (ROP ≤ -5.5 dBm).

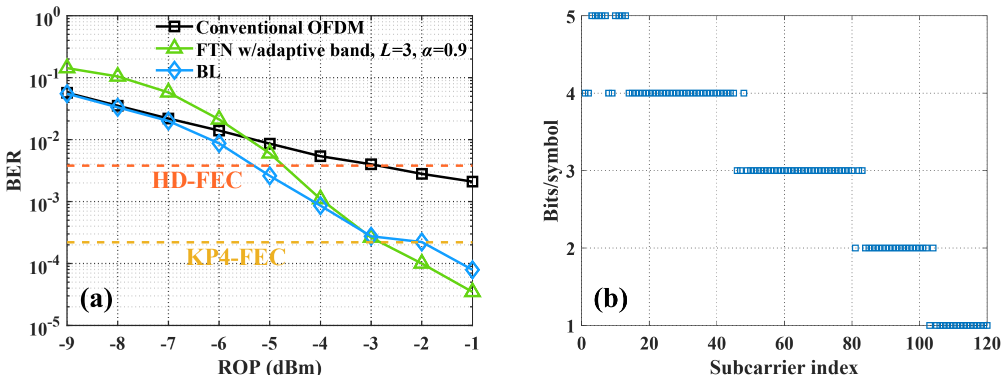

Fig. 9. (a) Measured ROP sensitivity curves ($L = 3$ for adaptive multi-band modulation), and (b) bits allocation result with the adaptive-loaded OFDM at ROP = −1 dBm.

5. Summary

We have proposed an adaptive multi-band modulation FTN scheme to make more rational use of the low-pass-like channel and reduce the computational complexity. The results of a 32.23-Gb/s and 20-km IM-DD optical transmission system have shown that the proposed scheme outperforms the conventional single-band FTN scheme while significantly reducing the implementation complexity. Specifically, when $L = 3$, the BER can be reduced from 5.04×10^{-4} to 2.54×10^{-4} and the corresponding complexity reductions are namely 92.65% in complex multiplication and 92.67% in complex addition, respectively. Due to the bandwidth saved in the high frequency (worst SNR), the proposed adaptive multi-band modulation FTN scheme has ~0.8-dB sensitivity improvement over the BL scheme at the KP4-FEC threshold. Apart from optical fiber systems, the proposed scheme is also feasible for other systems suffering from the steep frequency roll-off channel, for instance, VLC systems and underwater optical wireless transmission systems. Moreover, the performance of the proposed scheme could be further improved by jointly optimizing the sub-band number and the size of each sub-band, which will be studied in our future work.

Funding. Talent Fund of Beijing Jiaotong University (2024XKRC079); University Grants Committee (GRF 14205820).

Disclosures. The authors declare no conflicts of interest.

Data availability. Data underlying the results presented in this paper are not publicly available at this time but may be obtained from the authors upon reasonable request.

References

1. D. Che and X. Chen, "Modulation format and digital signal processing for IM-DD optics at post-200 G Era," J. Lightwave Technol. **42**(2), 588–605 (2023).
2. Z. Hu, Z. Zhou, C. K. Chan, *et al.*, "Equalizer state caching for fast data recovery in optically-switched data center networks," J. Lightwave Technol. **39**(17), 5362–5370 (2021).
3. L. K. Chen, Y. Shao, and Y. Di, "Underwater and water-air optical wireless communication," J. Lightwave Technol. **40**(5), 1440–1452 (2022).
4. R. Bonk, E. Harstead, R. Borkowski, *et al.*, "Perspectives on and the road towards 100 Gb/s TDM PON with intensity-modulation and direct detection," J. Opt. Commun. Netw. **15**(8), 518–526 (2023).
5. P. S. Chow, J. M. Cioffi, and J. A. C. Bingham, "A practical discrete multitone transceiver loading algorithm for data transmission over spectrally shaped channels," IEEE Trans. Commun. **43**(2/3/4), 773–775 (1995).
6. P. Song and D. Che, "Role of frequency-resolved SNR in entropy-loading DMT systems: rate comparison and simplified options," in *OFC* 2024, paper Th1J.6.
7. Z. Fan and J. Zhao, "Chirp-like polyphase sequence based discrete circulant transform spread OFDM for bandwidth-limited IM/DD systems," J. Lightwave Technol. **40**(8), 2283–2295 (2022).
8. G. Wang, P. Song, Y. Pan, *et al.*, "Secure OFDM-PON Bandwidth-limited System Precoded by Chaotic Frank Sequence-Based Circulant Matrix," in *CLEO* 2023, paper SF2 M.5.

Optics EXPRESS

9. T. Xu, S. Mikroulis, J. E. Mitchell, *et al.*, "Bandwidth compressed waveform for 60-GHz millimeter-wave radio over fiber experiment," J. Lightwave Technol. **34**(14), 3458–3465 (2016).
10. Z. Li, W. Wang, D. Zou, *et al.*, "DFT spread spectrally efficient frequency division multiplexing for IM-DD transmission in C-Band," J. Lightwave Technol. **38**(13), 3526–3532 (2020).
11. B. Yu, C. Guo, L. Yi, *et al.*, "150-Gb/s SEFDM IM/DD transmission using log-MAP Viterbi decoding for short reach optical links," Opt. Express **26**(24), 31075–31084 (2018).
12. Z. Hu and C. K. Chan, "Non-orthogonal matrix precoding based faster-than-Nyquist signaling over optical wireless communications," in *OFC* 2020, paper M1J.5.
13. J. Zhou, Y. Qiao, Z. Yang, *et al.*, "Capacity limit for faster-than-Nyquist non-orthogonal frequency-division multiplexing signaling," Sci. Rep. **7**(1), 3380 (2017).
14. M. Guo, Y. Qiao, J. Zhou, *et al.*, "ICI cancellation based on MIMO decoding for FTN non-orthogonal FDM systems," J. Lightwave Technol. **37**(3), 1045–1055 (2018).
15. S. Liu, J. Zhou, H. Wang, *et al.*, "Non-orthogonal DMT enabled by iterative ICI cancellation algorithm for bandwidth-limited IM/DD Optical Systems," J. Lightwave Technol. **40**(9), 2799–2806 (2022).
16. J. Zhou, Q. Sui, and Z. Li, "Non-orthogonal discrete multi-tone: toward higher spectral efficiency for optical networks," IEEE Commun. Mag. **59**(10), 70–75 (2021).
17. I. Darwazeh, T. Xu, T. Gui, *et al.*, "Optical SEFDM system; bandwidth saving using non-orthogonal sub-carriers," IEEE Photonics Technol. Lett. **26**(4), 352–355 (2013).
18. B. Yu, C. Guo, S. Zhang, *et al.*, "Chromatic dispersion mitigation using a SEFDM-based diversity technique for IM/DD long reach optical links," Opt. Express **27**(26), 38579–38592 (2019).
19. Y. Hong, J. Xu, and L. K. Chen, "Experimental investigation of multi-band OCT precoding for OFDM-based visible light communications," Opt. Express **25**(11), 12908–12914 (2017).
20. Z. Hu, S. Gao, Y. Shao, *et al.*, "A robust channel processor for faster-than-Nyquist Non-orthogonal FDM visible light communication systems," in *ECOC* 2018.
21. Y. Hong and L. K. Chen, "Toward user mobility for OFDM-based visible light communications," Opt. Lett. **41**(16), 3763–3766 (2016).
22. F. Khan, *LTE for 4 G mobile broadband: air interface technologies and performance* (Cambridge University, 2009), Chap. 9.
23. P. Song, Z. Hu, H. Chen, *et al.*, "Squared and rectangular QAM compatible decoder for spectrally efficient frequency division multiplexing optical systems," Opt. Laser Technol. **167**, 109776 (2023).